PAPER

Check for updates

Neighboring iron single atomic sites boost PtCo intermetallic activity for high-durability ORR electrocatalysis†

Kai Chen,[ab] Junheng Huang,[a] Junxiang Chen,[a] Jiyuan Gao,[ab] Zhiwen Lu,[ab] Xi Liu,[a] Senchen Lan,[c] Guohua Jia, ✦[d] Suqin Ci ✦[c] and Zhenhai Wen ✦[a]

Advancing fuel cell technology hinges on developing stable, efficient Pt-based catalysts for the oxygen reduction reaction (ORR), yet challenges like the high cost and limited durability of Pt-based materials persist. Here, we present an electrocatalyst that harnesses the strong interaction between Fe single atoms and neighboring ordered PtCo alloys (O-PtCo-FeNC) confined in microporous carbon. The unique coordination of FeN_3 sites with PtCo intermetallic compounds enables precise optimization of the catalyst size and structure, boosting PtCo intermetallic activity and yielding exceptional ORR performance. This is verified by a half-wave potential of 0.86 V *vs.* RHE in 0.5 M H_2SO_4 and a mass activity of 1.34 A mg_{Pt}^{-1}, which is an 8.1-fold improvement compared to that of Pt/C, while maintaining exceptional durability for over 50 000 cycles. *In situ* characterization and theoretical calculations reveal that isolated Fe sites reduce the d-band center of neighboring Pt sites, weakening adsorption energy and synergistically enhancing both activity and stability. When deployed in the air cathode of a hybrid acid/alkali Zn–air battery, the catalyst delivers an outstanding open circuit voltage of 2.32 V and a peak power density of 751 mW cm^{-2}. This integration of intermetallic compounds with single-atom sites establishes a new benchmark for advanced ORR electrocatalysts, marking a significant advancement in fuel cell technology.

Broader context

The development of efficient and durable electrocatalysts for the oxygen reduction reaction (ORR) is a cornerstone in advancing renewable energy technologies, particularly fuel cells and metal–air batteries. Nevertheless, the reliance on platinum (Pt)-based catalysts has hindered the widespread adoption of fuel cells due to their scarcity, high cost, and susceptibility to degradation under operational conditions. Innovative strategies are therefore needed to improve the activity, stability, and cost-effectiveness of Pt-based catalysts. To mitigate these limitations, we present a groundbreaking electrocatalyst that integrates ordered PtCo intermetallic compounds (IMCs) with Fe single-atom sites (O-PtCo-FeNC) embedded within a microporous carbon framework. The isolated FeN_3 units markedly boost the activity of neighboring PtCo IMCs, resulting in a mass activity that is 8.1 times greater than that of Pt/C while demonstrating exceptional durability for over 50 000 cycles. When applied in a hybrid acid/alkali Zn–air battery, the catalyst exhibited an outstanding open-circuit voltage of 2.32 V and a record peak power density of 751 mW cm^{-2}, setting a new benchmark for ORR catalysts. This study represents a significant advancement in electrocatalyst design by synergistically combining IMCs with single-atom sites, offering far-reaching implications for more efficient and sustainable renewable energy and fuel cell systems.

a State Key Laboratory of Structural Chemistry, and Fujian Provincial Key Laboratory of Materials and Techniques toward Hydrogen Energy, Fujian Institute of Research on the Structure of Matter, Chinese Academy of Sciences, Fuzhou, Fujian, 350002, China. E-mail: wen@fjirsm.ac.cn

b University of Chinese Academy of Sciences, Beijing, 100049, China

c Fujian Provincial Key Laboratory of Soil Environmental Health and Regulation, College of Resources and Environment, Fujian Agriculture and Forestry University, Fuzhou 350002, China. E-mail: sqci@fafu.edu.cn

d School of Molecular and Life Sciences, Curtin University, Bentley, WA 6102, Australia. E-mail: Guohua.Jia@curtin.edu.au

† Electronic supplementary information (ESI) available. See DOI: https://doi.org/10.1039/d5ee00624d

Introduction

Carbon-supported platinum catalysts show satisfying catalytic activity in various media, but scarcity and high cost of platinum prevent them from being widely employed in various fuel cells, such as proton exchange membrane fuel cells,[1,2] metal–air batteries,[3] organic fuel batteries, *etc.*[4] However, their appealing catalytic activity under acidic conditions, requiring a tiny over-potential to induce the ORR, continues to captivate the scientific community, propelling extensive research endeavours.[5,6] Researchers are endeavouring to enhance ORR activity through

6732 | *Energy Environ. Sci.*, 2025, **18**, 6732–6743

This journal is © The Royal Society of Chemistry 2025

strategies such as optimizing the nanostructure of PtM alloys (where M denotes a metal) and constructing core–shell structures.[7]

Alloying Pt with 3d transition metals (e.g., Fe, Co, Ni, and Cu) with smaller atomic radii effectively shifts the d-band center of Pt towards lower energies. This modification enables the optimization of oxygen intermediate adsorption/desorption behavior, accelerates the sluggish ORR kinetics, and enhances both the utilization efficiency and mass activity of Pt.[8,9] Taking PtCo alloy as an exemplar, despite its status as one of the most promising ORR catalysts, its potent catalytic capability cannot fully counteract operational instability, notably the dissolution of Co and the loss of alloy particles due to carbon matrix corrosion result in a reduction in catalytic activity due to changes in composition, structure, and geometry.[10,11] Consequently, in-depth investigation into the alloy structure and carbon support stability is imperative.[12,13] On the other hand, in contrast to disordered PtCo alloys (A1 structure), PtCo alloys with specific Pt/Co compositions can form ordered intermetallic structures. The strong 3d–5d orbital interaction between Co and Pt facilitates an ordered PtCo alloy, featuring a tetragonal $L1_0$ structure, and possessing hard magnetic characteristics.[14] This interaction mitigates cobalt leaching and comprehensively elevates catalytic activity and stability.[2] Regrettably, the ordering process of the alloy demands elevated temperatures, often resulting in the formation of larger nanoparticles that cannot provide adequate electrochemically active surface area for high mass activity. Hence, the ongoing challenges lie in the synthesis of PtCo intermetallic nanoparticles (NPs) with an optimal particle size through readily implementable strategies.[15,16]

Oxide coating, polymer coating, using KCl matrices, and various other approaches have been utilized to tackle the challenges.[17] Nevertheless, these strategies are still plagued by issues including inhomogeneous particle size and distribution, intricate procedures, and feeble interactions between NPs and carbon supports. Studies have shown that carbon supports play a crucial role in augmenting catalytic activity and stabilizing the nanoscale structure of alloys.[18,19] For example, in Liang's study, S–C bonds were formed on porous carbon matrices, and by exploiting the robust interaction between Pt and S, metal sintering at elevated temperatures was effectively mitigated, successfully synthesizing a series of small-sized Pt-based intermetallic compounds (IMCs).[20] Presently, owing to their abundant and modifiable porous architectures and diverse metal selections, a variety of metal–organic frameworks (MOFs) or zeolitic imidazolate frameworks (ZIFs) have been extensively employed for the production of porous carbon,[21] which in turn facilitates the deposition of small-sized IMCs. Nonetheless, smaller-sized nanoparticles possess higher surface energies, rendering them more prone to agglomeration, which subsequently accelerates the decline in activity.[22,23] In the context of catalyzing the ORR, single-atom catalysts (SACs), with Fe–N–C units serving as a notable exemplar (derived from MOFs, COFs), demonstrate outstanding performance.[24] Additionally, researchers have further observed that when Pt or Pt alloys are supported on carbon matrices abundant in M–N–C units, the reactivity and stability of the materials are markedly improved due

to distinctive synergistic effects.[25–28] The incorporation of single-atom sites (SASs) within fine pore structures promotes controlled growth of ordered alloys, uniform dispersion, the production of nanoparticles of optimal size, and the realization of synergistic enhancement of multiple catalytically active sites, thereby accelerating ORR kinetics.[26,29] Furthermore, metal atom doping within this structure fosters robust metal–support interactions, stabilizing the carbon matrix, anchoring alloy particles, and augmenting stability.[30,31] Although previous studies have examined the synergistic effects between SASs and Pt or Pt-based IMCs, the role of SASs in regulating the growth of IMC particles remains largely overlooked.[32] The ambiguity surrounding the key synergistic mechanisms, coupled with the persistent challenge of nanoparticle aggregation, necessitates further investigation.[29,33] Moreover, the precise localization of the active sites in these hybrid catalysts and the comprehensive elucidation of their catalytic mechanisms have yet to be achieved.[19,34]

Inspired by the aforementioned studies, we propose an innovative integrated catalyst comprising a Fe SAS-coordinated PtCo ordered alloy within a porous carbon structure. All-site calculations reveal that the incorporation of single-atom Fe generates a highly reactive interfacial microenvironment and lowers the d-band center of neighboring Pt, mitigating the excessive adsorption energy that would otherwise impede catalytic activity. The optimal integration of nanoscale dimensions, synergistic catalysis, and the stable nanostructure enables accelerated oxygen decomposition, resulting in exceptional catalytic activity and stability.

Results and discussion

Material synthesis and characterization

To synthesize porous carbon enriched with isolated iron sites for the deposition and subsequent reduction of Pt^{4+} and Co^{2+} which result in the formation of a PtCo ordered alloy, a zeolitic imidazolate framework (ZIF-8) was utilized as a molecular cage to encapsulate and isolate the metal precursor $Fe(acac)_3$. Subsequently, pyrolysis was performed to obtain the desired carbon support with Fe atomic sites (Fig. S1, ESI†).[35] As depicted in Fig. 1a, during the heating process, entropy governed the diffusion and reduction of Pt and Co atoms, leading to the formation of a single-phase solid solution of PtCo with the anticipated stoichiometric ratio.[36] In the cooling process, enthalpy facilitated the phase transition from the solid solution to an atomically ordered structure.[37] Throughout the process, the highly dispersed single atomic Fe on the carbon matrix attracted adjacent Pt and Co precursors, resulting in the formation of ultrafine PtCo IMCs coordinated by iron sites. In addition, the high-temperature pyrolysis of ZIF-8 and Fe-ZIF-8 produced a porous carbon skeleton with a rough surface, as depicted in Fig. S2 and S3 (ESI†), which enhances the dispersion and deposition of nanoparticles.[27,38] Consequently, under the combined effect of the two, the average diameter of the nanoparticles in PtCo-FeNC is reduced to 3.6 nm (Fig. 1b and Fig. S4, ESI†). Conversely, employing NC as the carrier results in a weaker confinement effect, enlarging the particle diameter to 5.1 nm (Fig. S5 and S6, ESI†). It is
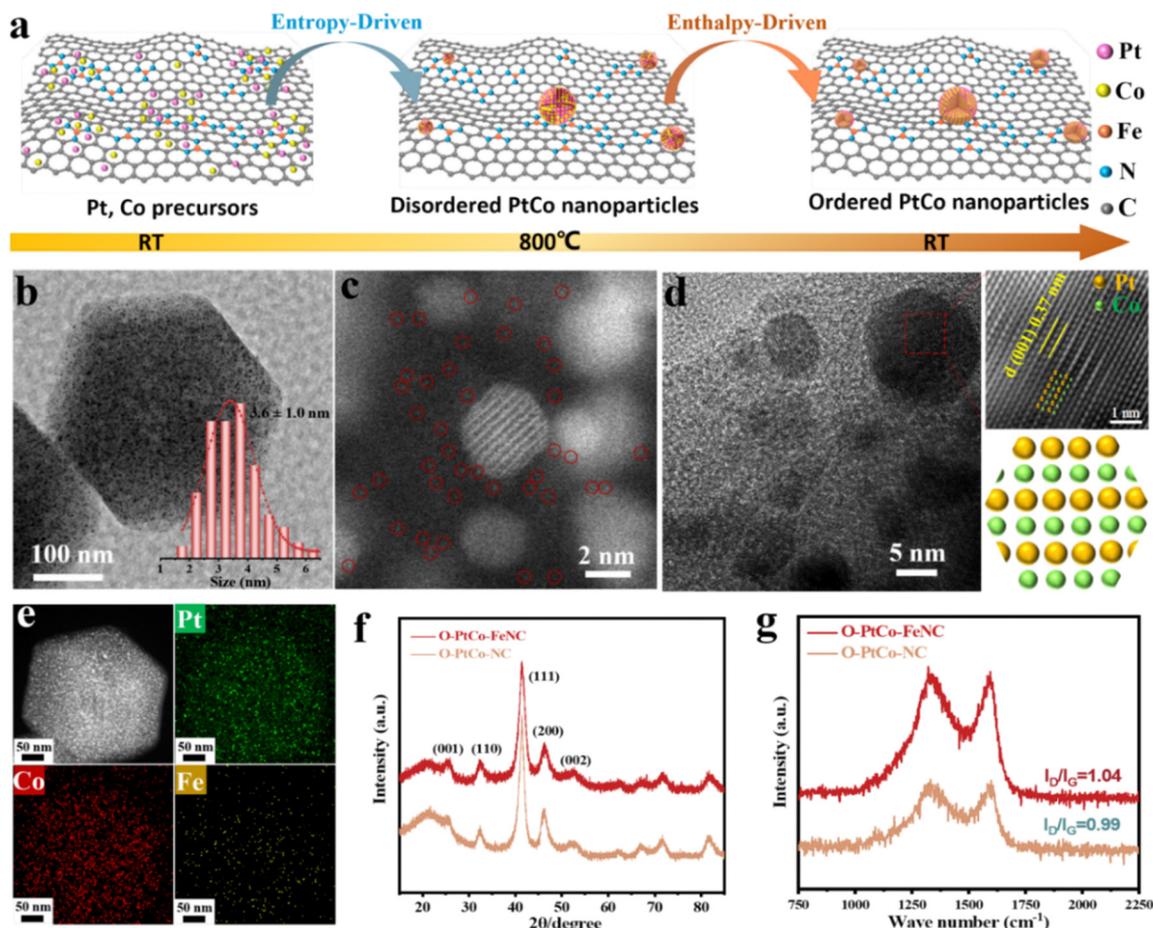
This journal is © The Royal Society of Chemistry 2025

Energy Environ. Sci., 2025, **18**, 6732–6743 | **6733**

Fig. 1 (a) Schematic diagram of the formation mechanism of ordered PtCo NPs on FeNCs; (b) low-magnification TEM image and histogram of particle diameters of O-PtCo-FeNC calculated from more than 200 particles; (c) aberration-corrected HAADF-STEM image; and (d) HRTEM and selected area FFT images. A schematic illustration below shows the orderly arrangement of Pt and Co atoms; (e) EDS-mapping image of O-PtCo-FeNC; (f) X-ray diffraction pattern of the obtained O-PtCo-FeNC and O-PtCo-NC; and (g) Raman spectra of O-PtCo-FeNC and O-PtCo-NC.

essential to highlight that at a lower reduction temperature (600 °C), the atomic arrangement within the PtCo alloy does not achieve orderliness. However, the growth-limiting influence of the single-atom carrier persists, restricting the particle size to approximately 2.6 nm (Fig. S7–S9, ESI†). The spherical aberration electron microscopy image in Fig. 1c shows that highly dispersed nanoparticles coexist with atomically dispersed Fe sites embedded in carbon. Analysis of high-resolution transmission electron microscopy (HR-TEM) images (Fig. 1d and Fig. S10a, b, ESI†) reveals lattice fringes measuring 0.37 nm and 0.217 nm, aligning closely with the ordered PtCo alloy's (001) and (111) planes.[14] The fast Fourier transform (FFT) pattern and the schematic atomic arrangement demonstrate the superlattice reflection corresponding to the (001) plane, where alternating brighter (Pt) and darker (Co) atoms are stacked in one direction, clearly showing the order of the Pt/Co atoms and confirming the formation of ordered PtCo on the Fe single atom support at 800 °C.[10] Energy-dispersive X-ray spectroscopy (EDS) elemental mapping images (Fig. 1e and Fig. S10c, ESI†) illustrate the uniform dispersion of Pt, Co, and Fe atoms on the carbon matrix. The superlattice peaks observed in Fig. 1f for O-PtCo-FeNC and O-PtCo-NC, approximately at 24.0 and 33.3,

correspond to the ordered (001) and (110) planes of the face-centered tetragonal (fct, JCPDS No. 65-8969) structure, adopting an ordered tetragonal structure in the space group of $P4/mmm$.[39,40] The corresponding Raman spectra indicate a higher I_D/I_G ratio for O-PtCo-FeNC compared to O-PtCo-NC, suggesting potentially higher catalytic activity for the material. Inductively coupled plasma atomic emission spectroscopy (ICP-AES) results for O-PtCo-FeNC reveal a Pt loading of *ca.* 8.9 wt%, with a Pt/Co atomic ratio nearing 48 : 52, and a Fe weight content of *ca.* 0.83 wt%.

X-ray photoelectron spectroscopy (XPS) was adeptly employed to elucidate the intricate electronic structure of O-PtCo-FeNC and O-PtCo-NC, as depicted in Fig. S11 (ESI†). In the Pt high-resolution spectrum of O-PtCo-FeNC, two prominent peaks at 71.6 and 74.9 eV were identified, corresponding to the metallic states of Pt $4f_{7/2}$ and $4f_{5/2}$, respectively. Intriguingly, the emergence of peaks at 72.4 and 75.8 eV confirms the presence of oxidized Pt forms (Fig. 2a).[41] A comparative analysis with O-PtCo-NC unveils that the introduction of iron atoms imparts a subtle negative shift in Pt^{2+}, a phenomenon attributable to the synergistic interaction between the PtCo alloy and Fe–N groups.[42] This shift is hypothesized to modulate the charge density of the core

6734 | *Energy Environ. Sci.*, 2025, **18**, 6732–6743
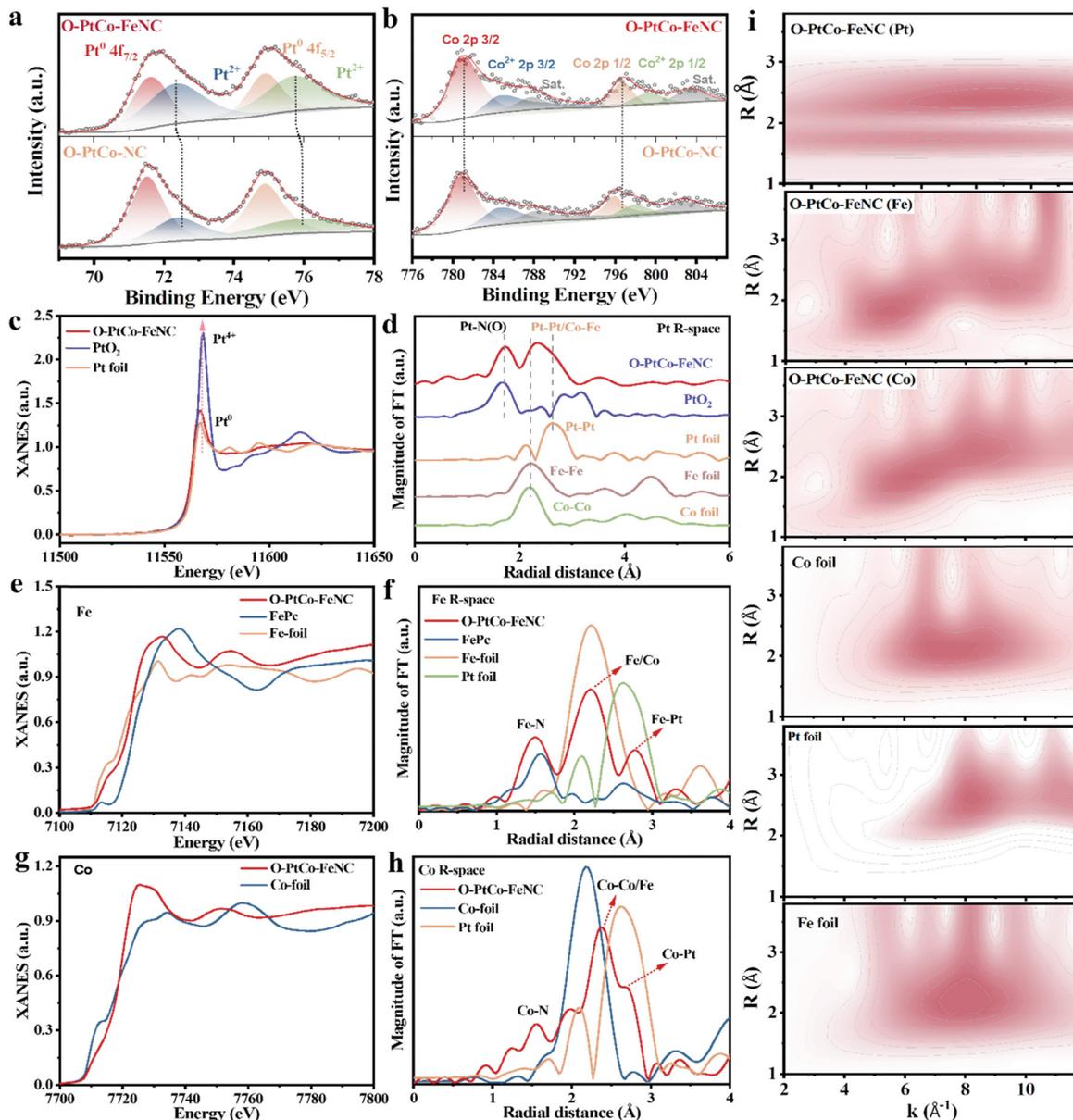
This journal is © The Royal Society of Chemistry 2025

Fig. 2 (a) and (b) Pt and Co XPS spectra of O-PtCo-FeNC and O-PtCo-NC; XANES and FT-EXAFS spectra of (c) and (d) Pt, (e) and (f) Fe, and (g) and (h) Co in O-PtCo-FeNC; and (i) wavelet transform EXAFS spectra of Pt, Co and Fe in O-PtCo-FeNC, Pt foil, Co foil and Fe foil.

metal ions,[43] as further evidenced by Fig. S12 (ESI†), which also reveals the coexistence of +2 and +3 iron oxidation states. Delving into Fig. 2b, the high-resolution XPS spectra of Co 2p in the O-PtCo-FeNC catalyst reveal two salient peaks at 781.1 and 796.6 eV, corresponding to Co $2p_{3/2}$ and Co $2p_{1/2}$, respectively.[44] Complementarily, the peaks residing at 784.9 and 799.4 eV are attributed to the Co^{2+} $2p_{3/2}$ and $2p_{1/2}$ states.[45] Significantly, a comparative study with O-PtCo-NC samples showcases a distinct positive shift in the Co binding energy, a shift that augurs well for enhanced catalytic activity, predominantly driven by the integration of Fe–N bonds. The C 1s spectrum, through meticulous deconvolution, unfolds into three discrete peaks. The central peak at 284.8 eV, characteristic of C–C bonds, is flanked by peaks at 285.6 and 287.6 eV, ascribed to C–N and C=N functional groups,

respectively (Fig. S13, ESI†).[46–48] Fig. S14 (ESI†) offers a glimpse into the N 1s spectrum, deconvoluted into pyridine, pyrrole, and graphitized nitrogen peaks at 398.7, 401.1, and 402.8 eV, respectively. Notably, the integrated area of the obvious metal–nitrogen bonds (Fe–N, Co–N) at 399.8 eV increases after the introduction of Fe atoms, indicating a stronger metal–support interaction.[49] The robust metal carrier, which facilitates the electron transfer in the ORR process through a M–N/C coordination interaction, plays a pivotal role in enhancing both the catalytic activity and stability.[15,23,50]

X-ray absorption spectroscopy (XAS) was subsequently utilized to further demystify the electronic state and local coordination environment of the catalyst. Fig. 2c reveals that Pt in O-PtCo-FeNC exists in a lower oxidation state and adopts a

metallic configuration, as evidenced by the white line intensity (~11 567 eV) in the X-ray absorption near-edge structure (XANES) spectrum, which closely resembles that of Pt foil. The prominent peak observed at the Pt L3-edge in the Fourier-transformed extended X-ray absorption fine structure (FT-EXAFS) spectrum of O-PtCo-FeNC, centered around 1.7 Å, suggests the presence of Pt–O or Pt–N coordination.[51] Concurrently, the scattering feature at ~2.3 Å is attributed to Pt–Pt/Co/Fe bonding interactions (Fig. 2d).[50] These observations correlate with the dual-center contributions identified in the wavelet-transformed EXAFS spectrum (Fig. 2i). Analyzing the Fe K-edge spectra in O-PtCo-FeNC, with Fe foil and FePc serving as benchmarks, revealed intriguing insights (Fig. 2e). The absorption edge of O-PtCo-FeNC, nestled between the spectra of FePc (incorporating the Fe(III)–N4 moiety) and Fe foil, implies that the iron atoms possess a positive charge,[15,23] in harmony with the XPS findings. The shoulder peak near 1.5 Å in Fig. 2f, a testament to the Fe–N bonds in the carbon carrier, unequivocally confirms the existence of single-atom iron,[35] with an average coordination number of 2.8 (Fig. S15a and Table S1, ESI†). Peaks observed between 2–3 Å are indicative

of metal bonds formed between Fe and Pt/Co.[10,38,52] As shown in Fig. 2i, Fe K-edge radial distribution function, exhibiting maximum intensity at 5.5 and 9.3 Å^{-1}, is attributed to single-atom iron and Fe–Co/Pt bonds.[53,54] The Co XANES spectra of O-PtCo-FeNC, devoid of a white line near Co foil (Fig. 2g) and showing a slight peak shift towards higher energy relative to Co foil, suggest that Co atoms bear a positive charge.[1,49] This finding implies a robust interaction between Pt and Co within the ordered alloy particles.[55] Fig. 2h and Fig. S15b (ESI†) present EXAFS fitting spectra that disclose a Co–N peak at 1.9 Å and abundant coordinated Co–Co/Fe and Co–Pt peaks at 2–3 Å.[10] The corresponding fitting parameters are shown in Table S2 (ESI†). Furthermore, the Co wavelet transform spectra conspicuously display features linked to Co-Co/Fe and Pt-Co bonds, enriching our understanding of the catalyst's intricate structure. These findings demonstrate direct interfacial interactions between Pt and Co in the PtCo ordered alloy with FeN3 sites embedded within the porous carbon matrix, establishing a critical foundation for synergistic enhancement of both catalytic activity and operational stability.
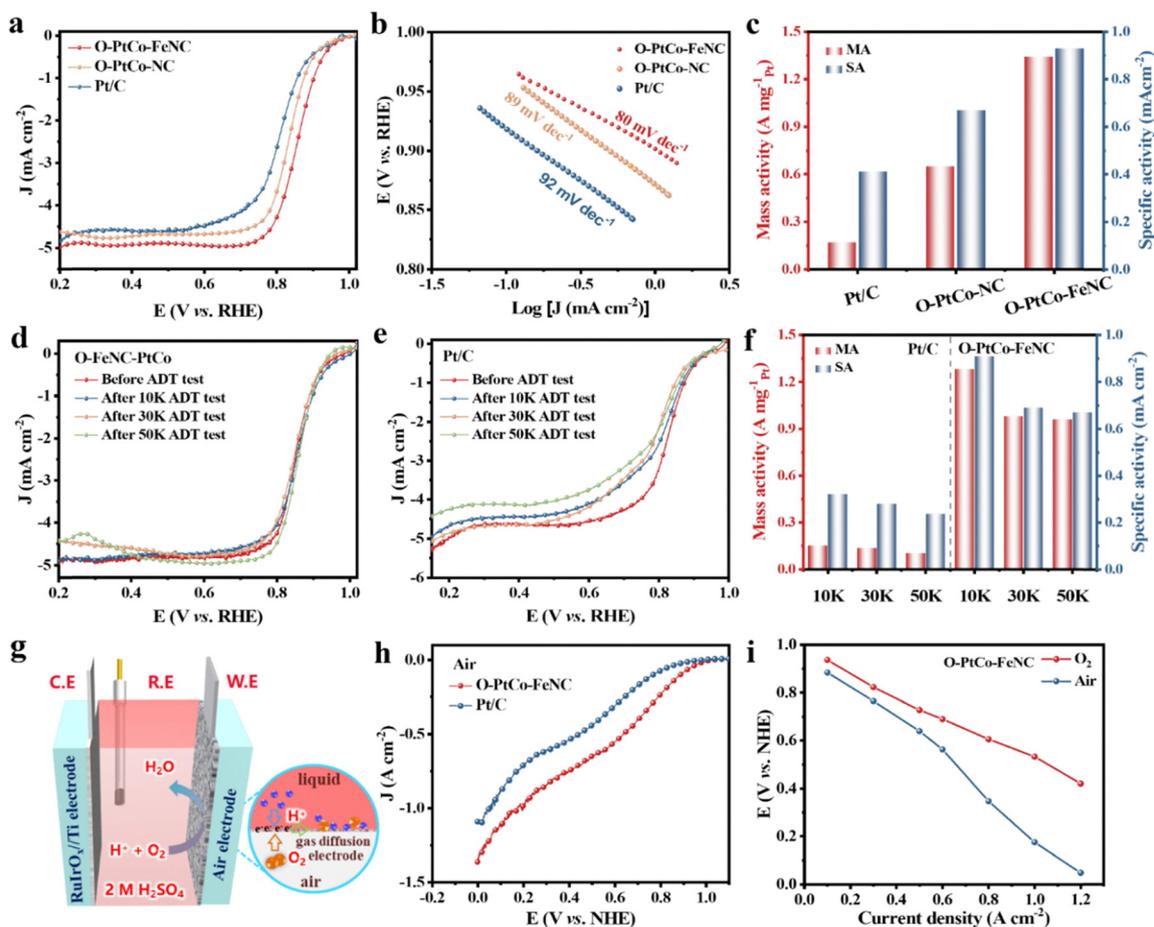

Fig. 3 (a) ORR polarization plots for Pt/C, O-PtCo-NC and O-PtCo-FeNC; (b) Tafel plots of the corresponding catalysts; (c) mass activity and specific activity of Pt/C and O-PtCo-FeNC at 0.85 V *vs.* RHE; (d) and (e) LSVs of Pt/C and O-PtCo-FeNC before and after the ADT; and (f) mass activity and specific activity of Pt/C and O-PtCo-FeNC before and after ADT at 0.85 V *vs.* RHE. (g) Schematic diagram of a three-electrode test of the ORR based on a gas diffusion electrode (GDE). (h) Polarization curves based on the GDE of Pt and O-PtCo-FeNC catalysts in the air environment. (i) Comparison of O-PtCo-FeNC curves under different current densities in air and O2 environments.

6736 | *Energy Environ. Sci.,* 2025, **18**, 6732–6743

This journal is © The Royal Society of Chemistry 2025

Electrochemical performance for the ORR

To elucidate the oxygen reduction activity of the synthesized catalyst, we employed a three-electrode setup, immersing it in a 0.5 M H_2SO_4 solution saturated with oxygen. Fig. S16 (ESI†) reveals that the precursor, FeNC, adorned with uniformly distributed iron sites, showcases a half-wave potential of 0.74 V. This value surpasses that of the NC, highlighting the potential of integrating ordered alloys to amplify ORR activity. The electrochemical prowess of O-PtCo-FeNC is further evidenced in its polarization curve, which boasts an initial potential of 1.0 V and an impressive half-wave potential of 0.86 V. These values are notably superior to those of O-PtCo-NC (0.98 V and 0.84 V) and Pt/C (0.98 V and 0.81 V), as delineated in Fig. 3a and Fig. S17a (ESI†). Additionally, the relatively smaller Tafel slope of 82 mV dec^{-1} for O-PtCo-FeNC underscores a swifter kinetic rate, a testament to its enhanced catalytic efficiency (Fig. 3b).[56] Notably, the considerable difference between the half-wave potentials of O-PtCo-FeNC and O-PtCo-NC indicates that the enhancement of its ORR activity is due to the synergistic action of the ordered alloy and Fe SASs. Delving deeper into the reaction mechanism, both the Koutecky–Levich (K–L) equation and rotating ring-disk electrode (RRDE) results, presented in Fig. S17b–d and Fig. S18 (ESI†), affirm the predominance of a four-electron transfer mechanism across a potential range of 0.1–0.9 V for both Pt/C and O-PtCo-FeNC. In addition, the unique synergy has been confirmed between the disordered PtCo alloy and the Fe–N unit (Fig. S19, ESI†). Because of the optimization of the size of nanoparticles, abundant active sites are exposed, thereby expanding the electrochemically active area. O-PtCo-FeNC offers a significantly increased mass activity (1.34 A mg$_{Pt}^{-1}$) and specific activity (0.93 mA cm^{-2}), which is 8.1 times and 2.3 times that of commercial Pt/C, respectively (Fig. 3c). Simultaneously, its values surpass those of ordered alloys without the assistance of Fe single atoms. In parallel to catalytic activity, long-term stability emerges as a pivotal evaluation criterion. In Fig. 3d, the accelerated durability test (ADT) indicates the extraordinary robustness of O-PtCo-FeNC in acidic media. After enduring 50 000 cycles, the self-developed catalyst maintains a high half-wave potential with a negative shift of only 8 mV, in stark contrast to the 50 mV shift observed for Pt/C (Fig. 3e). As demonstrated in Table S3 (ESI†), the PtCo ordered alloy catalyst with isolated iron-anchored sites exhibits superior mass activity and exceptional stability in H_2SO_4 media. In addition, in Fig. 3f, in contrast to the obviously diminished mass activity of Pt/C (59%), the reinforced material maintains 72% mass activity. To meticulously analyze the catalysts' alterations during the cycle process, we recorded CV curves, electric double-layer capacitance, and electrochemical impedance (Fig. S20–S24, ESI†). O-PtCo-FeNC differs significantly from Pt/C under the same conditions, indicating that the stronger metal–nitrogen–carbon structure not only increases the stability of the carbon framework and synergistically boosts the catalytic activity, but also imparts the ordered PtCo alloy with firm structural stability and catalytic stability.

To evaluate the activity of commercial Pt/C and the Fe single-atom synergistic IMCs in sulfuric acid media (2.0 M) under practical conditions with greater precision, we constructed a three-electrode setup based on a gas diffusion electrode (GDE),[57] as illustrated in Fig. 3g. The polarization curve (Fig. 3h) illustrates that within a practical battery setting, the O-PtCo-FeNC catalyst initiates the oxygen reduction reaction at 1.0 V (vs. NHE), yielding a reduction current surpassing that of platinum carbon throughout the negative scan process. Subsequently, as shown in Fig. S25a (ESI†), the O-PtCo-FeNC catalyst operates at 0.77, 0.64, and 0.18 V to achieve current densities of 0.3, 0.5, and 1.0 A cm^{-2}, respectively, exhibiting an enhancement of more than 0.16 V as compared to a commercial material. These findings demonstrate that O-PtCo-FeNC exhibits a greater propensity to generate high current density at elevated potentials, hence contributing to increased power density. This disparity in activity is also present in the GDE test involving oxygen supply. Notably, at a current density of 1.0 A cm^{-2}, the O-PtCo-FeNC catalyst necessitates an overpotential of 0.18 V lower than that of platinum carbon (Fig. S25b and c, ESI†). Furthermore, the comparative analysis in Fig. 3i reveals that during operation at high current densities (>0.6 A cm^{-2}), rapid consumption of air's oxygen leads to insufficient supply, limiting mass transfer, and subsequently requiring a lager potential to maintain the same current increase. However, upon adequate oxygen supply, it satisfies the demands for operating at high current. The air cathode tests conducted under realistic conditions affirm the potential of the Fe single-atom coordinated PtCo ordered alloy as a high-performance cathode for hybrid Zn–air batteries.

In situ characterization

To elucidate the catalytic mechanism, in situ attenuated total reflection-surface enhanced infrared absorption spectroscopy (ATR-SEIRAS) was employed to monitor the intermediates during the ORR. As shown in Fig. S26a (ESI†), the catalyst was uniformly coated onto an Au thin film on an Si prism and further assembled into a three-electrode system for ORR testing in O_2-saturated 0.5 M H_2SO_4 solution. The reference spectrum was collected at 1.2 V, and the oxygen-containing intermediates on the catalyst were tested under a potential scan from 1.1 to 0 V. Fig. 4a and Fig. S26b (ESI†) show that O-PtCo-NC displays readily identifiable peaks for OOH* and HOOH* at 1261 cm^{-1} and 1407 cm^{-1}, respectively, indicating that the associative pathway dominates the ORR on its surface.[58,59] Meanwhile, the presence of HOOH* suggests hindered hydrogen dissociation of OOH*, which is detrimental to catalytic activity and stability. After introducing FeN$_3$ units onto the carbon matrix supporting ordered PtCo alloy particles, a peak appears at 1457 cm^{-1} in the infrared spectrum attributed to the O–O stretching mode of *O_2 (Fig. 4b and Fig. S26c, ESI†).[60,61] This demonstrates that the ORR pathway on the O-PtCo-FeNC surface is predominantly associative. Ultimately, an in situ Raman spectroelectrochemical device featuring a gas–solid–liquid interface is employed to analyze the signals of surface-related compounds in the target samples at various potentials (Fig. S27a, ESI†). The Raman peak at 980 cm^{-1}, associated with the symmetric stretching vibration of SO_4^{2-}, remained constant, as depicted in Fig. 4c. The peak located around 890 cm^{-1} is attributed to the stretching vibration of oxygen species (*O). The accumulation of *O can be ascribed to the rapid dissociation of *OOH at the Pt sites of the PtCo ordered
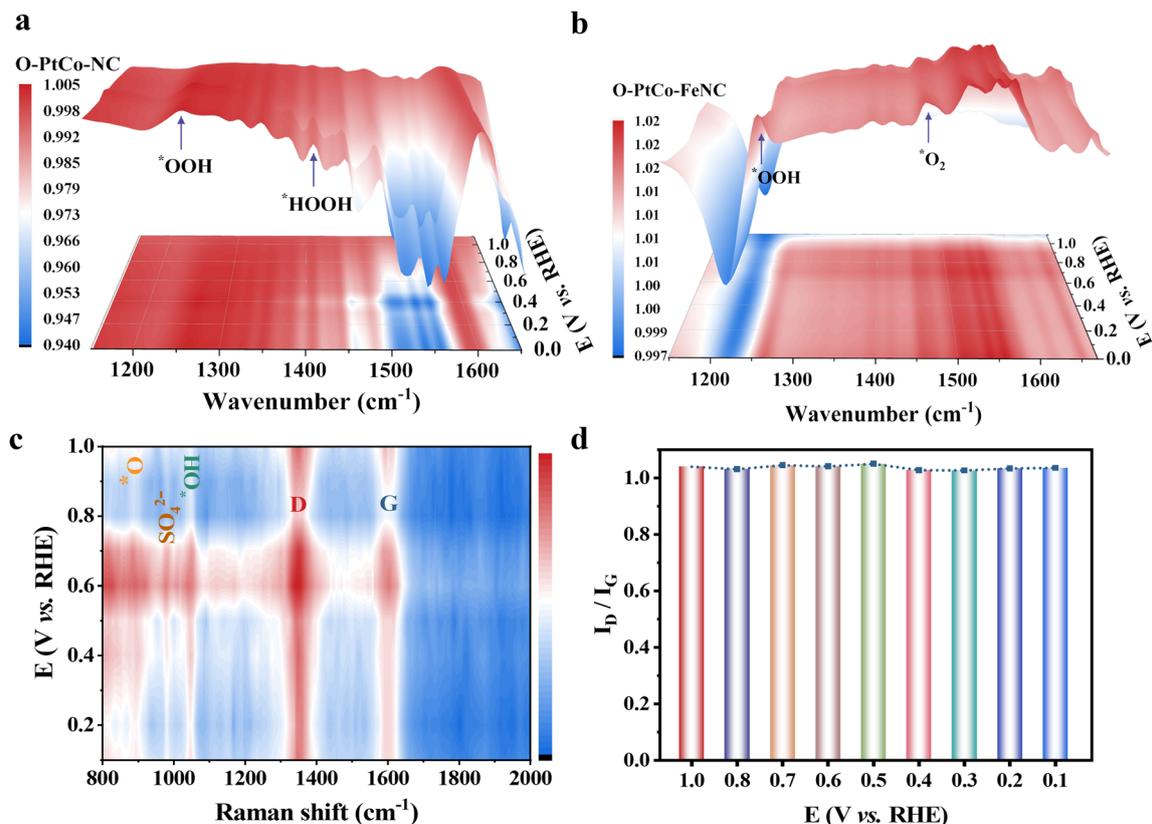
Fig. 4 (a) Three-dimensional *in situ* ATR-FTIR spectrum of O-PtCo-FeNC in O_2-saturated 0.5 M H_2SO_4; (b) *in situ* ATR-FTIR spectrum of O-PtCo-FeNC; (c) two-dimensional *in situ* Raman spectroscopy signals at different potentials of O-PtCo-FeNC; and (d) I_D/I_G changes during *in situ* Raman testing.

alloy modified with iron SASs, forming *O intermediates. This is a crucial step in the four-electron ORR. The emergence of a new peak at 1048 cm^{-1} corresponds to the *OH adsorbed on active sites, respectively (Fig. 4c and Fig. S27b, ESI†).[62,63] *In situ* ATR-SEIRAS and Raman results revealed oxygen intermediates detected on O-PtCo-FeNC, confirming that the introduction of Fe single atoms accelerated the ORR on the surface of the PtCo ordered alloy. Notably, in Fig. 4d, the G and D main peaks remained consistent across the spectrum, indicating that the appearance of new peaks originates from O groups involved in the electrocatalytic process rather than alterations in the carbon structure.

Theoretical calculations and analysis

Theoretical simulations based on first-principles methods were employed to investigate the effect of single-atom Fe sites on the ORR catalytic activity of ordered PtCo alloys. Given that the system encompasses interfaces, alloys, and doping, the diversity of exposed sites is extensive. Consequently, it is crucial to account for this diversity in the simulation process and to calculate as many possible sites as feasible. To address this, the machine learning potential (MLP) was utilized to simulate the interface through annealing.[64] Additionally, in conjunction with the large atom model (LAM),[65,66] we examined the reaction activity of all possible exposed sites (Fig. 5a). The annealing simulations of the ordered PtCo alloy with atomically dispersed

Fe sites and the ordered PtCo alloy on the NC substrate were conducted for a total of 150 picoseconds, and the corresponding snapshots are presented in Fig. 5b and Fig. S28 (ESI†). Based on these simulations, activity of all sites was calculated. The computational hydrogen electrode (CHE) method was employed to address the charged species,[67] and the virtual energetic span (δE^v) was used as the determinant of activity.[68] Fig. 5c and Fig. S29 (ESI†) show a colormap of virial displaying the results of the all-site calculations, with light green and dark green representing high-activity and low-activity sites, respectively. The total system activity is the aggregate of all sites. To clarify the relationship between the sites and activity, the activity of each site is plotted in Fig. S30 (ESI†). The horizontal axis represents the δE^v value of the activity (its relationship with the turnover frequency (TOF) of the ORR at a given site is given as, TOF = $k_0 \exp(-\delta E^v/RT)$, where k_0 is the standard reaction kinetic constant for the ORR, indicating that a higher δE^v corresponds to higher activity). The dotted line illustrates the activity ranking from high to low. Consequently, it is evident that the total activity value satisfies O-PtCo-FeNC > O-PtCo-NC, aligning with the experimental results.

Moreover, nearly 95% of the activity is attributed to 2–4% of the active sites, underscoring the necessity for comprehensive site calculations. Additionally, to assess the influence of potential, we obtained results at multiple potentials ranging from 0.7 to 1.12 V and constructed a Tafel curve. The curve
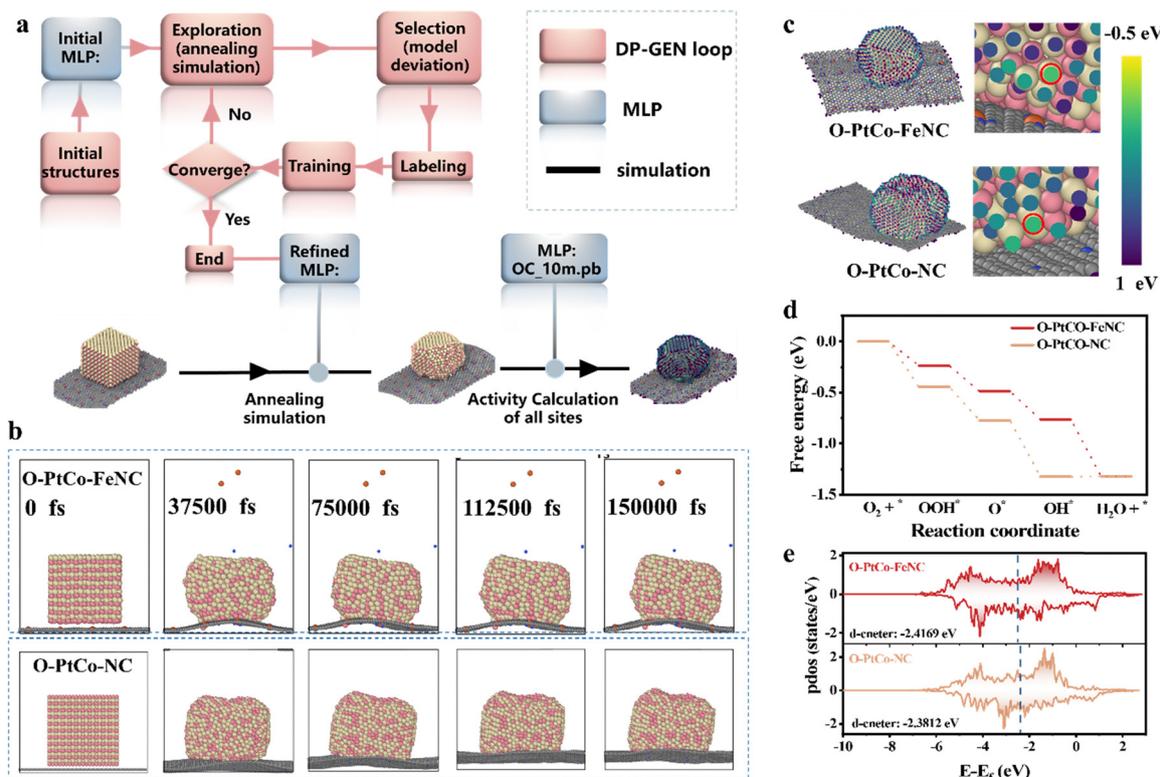
Fig. 5 (a) A schematic workflow for the simulations and reaction activity calculations; (b) representative snap shots of the MD process; and (c) the spatial distribution of activities in each site. The color indicates the associated δE^v value. The most active sites are highlighted by red circles. (d) The FED of the most active sites; (e) the pdos and d-band centers in the most active sites.

demonstrates that O-PtCo-FeNC consistently outperforms O-PtCo-NC at each potential (Fig. S31, ESI†), which is consistent with the experimental findings and further validates the accuracy of the computational results. To analyze the sites and elucidate the underlying cause of the variation in catalytic activity of ordered PtCo alloys on different carbon matrices, we accurately extracted the active site and constructed its free energy diagram (FED). Fig. 5d shows that the maximum Gibbs free energy differences (ΔG_{max}) for the PtCo IMCs and PtCo coordinated by SASs are 0.0026 eV and −0.23 eV, respectively, indicating that O-PtCo-FeNC exhibits significantly superior performance. Additionally, O-PtCo-FeNC shows stronger adsorption, suggesting that the FeN$_3$ unit in catalysis functions to decrease the reactivity of the PtCo interface, resulting in weaker adsorption and enhanced activity. The partial density of states (pdos) analysis in Fig. 5e reveals that the d-band center of Pt in the PtCo IMC is lowered upon doping with a single iron atom, which is a key factor in its reduced adsorption. The spatial charge difference analysis reveals electron withdrawal from the PtCo phase and accumulation at FeN$_3$ sites (Fig. S32a and b, ESI†). In the atomic charge difference analysis, Fe undergoes a critical loss of electrons, whereas the reactive Pt gains electrons (Fig. S32c, ESI†). This indicates that the overall charge transfer stems from remote induction between Fe and Pt during phase overlap, which elevates the electrostatic potential of Fe while lowering that of Pt. Consequently, electrons migrate from the PtCo phase to Pt and from the FeN$_3$ phase to Fe to

compensate for this electrostatic potential imbalance. The resulting intense electrostatic microenvironment, characterized by localized charge polarization, creates a highly reactive zone. Theoretically, the formation of such induced electrostatic potential pairs at the phase junction significantly increases the probability of formation of favorable reaction pathways, thereby enhancing catalytic activity. Thus, the role of FeN$_3$ sites in O-PtCo-FeNC catalysts for the ORR can be summarized as follows: first, FeN$_3$ sites do not act directly as active sites, but synergize with the PtCo phase to establish a highly reactive interfacial microenvironment, indirectly augmenting the catalytic activity of the PtCo component. Second, Fe atoms lower the d-band center of the Pt site, weakening the initially strong adsorption and thereby improving catalytic activity.

Electrochemical performance of hybrid acid/alkali Zn–air batteries

A schematic of a flow hybrid acid/alkali battery is displayed in Fig. 6a. Specifically, 4.0 M KOH and 2.0 M H$_2$SO$_4$ were utilized as the Zn anode and the ORR catholyte, respectively, and a cation-exchange membrane was employed to separate the electrolyte and enable ion movement during the discharge process.[69] This one-of-a-kind battery structure is ingeniously designed to fully harness the electrochemical neutralization energy, thereby significantly elevating both the working voltage and energy density of Zn–air batteries.[70,71] Furthermore, the acidic cathode medium effectively precludes the carbonation of
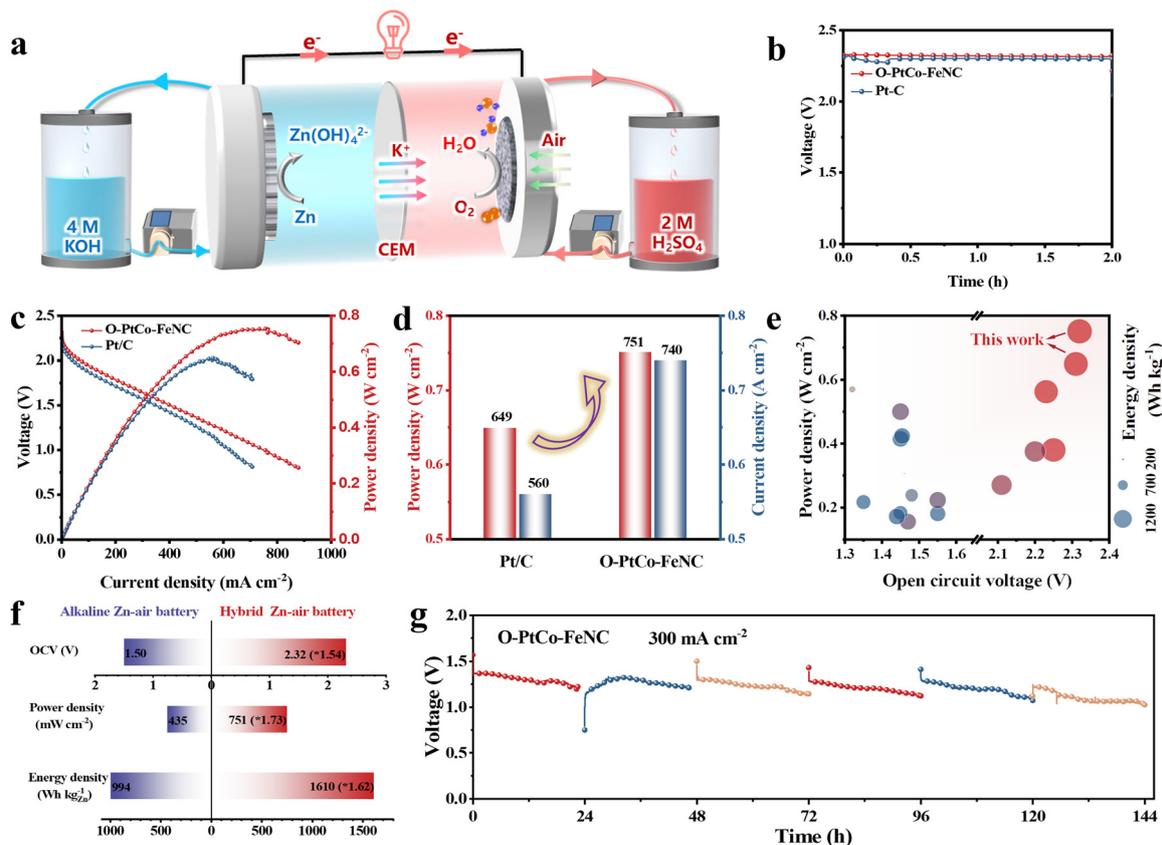
Fig. 6 (a) Schematic diagram of the hybrid acid/alkali Zn–air battery; (b) open circuit voltage of devices with O-PtCo-FeNC and Pt/C as the air cathode; (c) discharge polarization curve and power density of the hybrid battery device with two catalysts; (d) comparison diagram of maximum power density and the corresponding current density of two batteries; (e) comparing the open circuit voltage, power density, and energy density of the hybrid Zn–air battery with the values reported in the literature; and (f) performance comparison of conventional alkaline Zn–air batteries and hybrid acid/alkali Zn–air batteries equipped with O-PtCo-FeNC as the air cathode. (g) Battery discharge stability test at 300 mA cm^{-2}.

the alkaline electrolyte, a common challenge in traditional battery systems. Fig. 6b shows that the hybrid Zn–air battery with O-PtCo-FeNC as the air cathode has an open-circuit voltage of 2.32 V and can power an LED array (Fig. S33, ESI†). Fig. 6c and d further corroborate this, showcasing the peak power density and the corresponding current density of O-PtCo-FeNC (751 mW cm^{-2}, 740 mA cm^{-2}), which are significantly superior to those of Pt/C (649 mW cm^{-2}, 560 mA cm^{-2}). When the cathode is supplied with high-purity oxygen, the self-assembled device exhibits a maximum power output of 850 mW cm^{-2}, outperforming those of commercially available devices (Fig. S34, ESI†). The hybrid battery, which is constructed with the atomic Fe-site coordinated ordered PtCo alloy catalyst, shows a mass specific capacity of 803 mA h g$_{Zn}^{-1}$ and an energy density of 1610 W h kg$_{Zn}^{-1}$ in constant current discharge tests at 20 mA cm^{-2} (Fig. S35, ESI†). From Fig. 6e and Table S4 (ESI†), it is evident that the hybrid acid/alkali Zn–air battery, which is equipped with the ordered PtCo alloy modified with atomic Fe-sites, shows open circuit voltage, peak power density, and energy density values outperforming the values reported in the literature. The exceptional outcome is a direct consequence of the attainment of superior catalytic efficacy and the inventive configuration of the Zn–air battery architecture.

The voltage profiles at various current densities, as depicted in Fig. S36 (ESI†), further underscore the superior discharge properties of batteries equipped with O-PtCo-FeNC. For comparison, we concurrently evaluated the ORR performance of Pt/C and O-PtCo-FeNC. As shown in Fig. S37 (ESI†), O-PtCo-FeNC also exhibits overall superior activity to that of commercial Pt/C under alkaline conditions. However, although the alkaline Zn–air battery constructed with O-PtCo-FeNC shows an open-circuit voltage of 1.5 V, a power density of 435 mW cm^{-2}, and an energy density of 959 W h kg$_{Zn}^{-1}$—already exceeding the performance of current alkaline Zn–air batteries—these metrics remain significantly lower than those exhibited by the hybrid battery (Table S4, ESI†). Devices based on the hybrid architecture demonstrate improvements of more than 1.5 times in these parameters (Fig. 6h). Additionally, the performance and stability of the hybrid battery at higher discharge current densities were also rigorously assessed. Remarkably, owing to the exceptional stability of our bespoke catalyst, the battery demonstrates stable operation for 144 hours at a current density of 300 mA cm^{-2} (Fig. 6g). Post-stability testing, the material retains its original phase and structural properties, with the particle size increasing by only 0.3 nm (Fig. S38 and S39, ESI†). Moreover, at lower current density, it exhibits reliable operation for approximately

6740 | Energy Environ. Sci., 2025, 18, 6732–6743

This journal is © The Royal Society of Chemistry 2025

400 hours (Fig. S40, ESI†). A series of battery activity experiments suggested that O-PtCo-FeNC has salient application potential in high-voltage hybrid acid/alkali Zn–air batteries.

While the hybrid acid/alkaline Zn–air battery demonstrates remarkable performance, challenges such as the continuous consumption of OH^- and H^+ ions at their respective electrodes, K^+ migration leading to K_2SO_4 formation, and the stringent stability requirements of catalytic materials in acidic environments could impact long-term stability. However, these limitations can be systematically addressed through strategies including (1) optimizing electrolyte composition to balance ion transport and suppress side reactions, (2) developing advanced acid-tolerant catalysts (e.g., FeN_3-stabilized PtCo intermetallic), (3) refining the battery architecture to enhance ion selectivity, and (4) implementing rigorous testing protocols under realistic operating conditions. The ultra-high power density (751 mW cm^{-2}) and operating voltage (2.32 V) of this hybrid system position it as an ideal candidate for high-power-demanding applications, such as grid-scale peak power plants and ultrafast electric vehicle charging stations. Notably, the acid-resistant cathode design eliminates carbonate precipitation—a critical failure mechanism in conventional alkaline Zn–air batteries—enabling reliable operation in humid or CO_2-intensive environments (e.g., offshore platforms and remote sensors). Furthermore, the potential to utilize recycled acidic/alkaline waste streams as electrolytes aligns with circular economy principles, reducing resource consumption and advancing sustainability goals.

Conclusions

In this study, we propose an innovative strategy to enhance the catalytic activity and stability of platinum-based catalysts for the oxygen reduction reaction by coordinating Fe–N–C sites onto ordered PtCo alloys within a porous carbon matrix. The unique FeN_3 isolated unit effectively lowers the d-band center of Pt, reducing excessive adsorption, which leads to an O-PtCo-FeNC catalyst exhibiting an impressive half-wave potential of 0.86 V. Its mass activity significantly surpasses that of commercial Pt/C catalysts, while maintaining excellent stability over 50 000 cycles. The catalyst's high activity was further validated through its use in a hybrid acid/alkali flow Zn–air battery, which exhibited a maximum power density of 751 mW cm^{-2}. This integrated design of single-atom and ordered alloy catalysts, coupled with an innovative battery architecture, paves the way for the development of advanced electrode materials and energy conversion devices.

Author contributions

K. Chen: conceptualization, formal analysis, investigation, writing – original draft, writing – review and editing; J. H. Huang, J. Y. Gao, Z. W. Lu, X. Liu and S. C. Lan: formal analysis, investigation, validation, and visualization; J. X. Chen: data curation, methodology, software, and writing – original draft; G. H. Jia: resources and writing – review and editing; S. Q. Ci: resources, supervision, and writing – review and editing; and Z. H. Wen: conceptualization, resources, supervision, and writing – review and editing.

Data availability

The data supporting this article have been included as part of the ESI.†

Conflicts of interest

There are no conflicts to declare.

Acknowledgements

References

1 L. Huang, M. Wei, R. Qi, C. L. Dong, D. Dang, C.-C. Yang, C. Xia, C. Chen, S. Zaman and F. M. Li, Nat. Commun., 2022, 13, 6703.

2 L. Chong, J. Wen, J. Kubal, F. G. Sen, J. Zou, J. Greeley, M. Chan, H. Barkholtz, W. Ding and D. J. Liu, Science, 2018, 362, 1276–1281.

3 G. Wang, J. Chang, S. Koul, A. Kushima and Y. Yang, J. Am. Chem. Soc., 2021, 143, 11595–11601.

4 J. Chang, G. Wang, C. Li, Y. He, Y. Zhu, W. Zhang, M. Sajid, A. Kara, M. Gu and Y. Yang, Joule, 2023, 7, 587–602.

5 D. Wang, H. L. Xin, R. Hovden, H. Wang, Y. Yu, D. A. Muller, F. J. DiSalvo and H. D. Abruna, Nat. Mater., 2013, 12, 81–87.

6 H. Y. Kim, J. M. Kim, Y. Ha, J. Woo, A. Byun, T. J. Shin, K. H. Park, H. Y. Jeong, H. Kim, J. Y. Kim and S. H. Joo, ACS Catal., 2019, 9, 11242–11254.

7 S. L. Xu, S. C. Shen, S. Zhao, Y. W. Ding, S. Q. Chu, P. Chen, Y. Lin and H. W. Liang, Chem. Sci., 2020, 11, 7933–7939.

8 L. Bu, Q. Shao, B. E. J. Guo, J. Yao and X. Huang, J. Am. Chem. Soc., 2017, 139, 9576–9582.

9 L. Huang, H. Niu, C. Xia, F. M. Li, Z. Shahid and B. Y. Xia, Adv. Mater., 2024, 36, 2404773.

10 Q. Cheng, S. Yang, C. Fu, L. Zou, Z. Zou, Z. Jiang, J. Zhang and H. Yang, Energy Environ. Sci., 2022, 15, 278–286.

11 W. Zhao, B. Chi, L. Liang, P. Yang, W. Zhang, X. Ge, L. Wang, Z. Cui and S. Liao, ACS Catal., 2022, 12, 7571–7578.

12 Y. Wang, L. Sun, H. Lv, C. Zheng and B. Liu, CCS Chem., 2023, 5, 1896–1907.

13 Y. T. Pan, D. Li, S. Sharma, C. Wang, M. J. Zachman, E. C. Wegener, A. J. Kropf, Y. S. Kim, D. J. Myers and A. A. Peterson, Chem. Catal., 2022, 2, 3559–3572.

This journal is © The Royal Society of Chemistry 2025

Energy Environ. Sci., 2025, 18, 6732–6743 | 6741

14 J. Li, S. Sharma, X. Liu, Y. T. Pan, J. S. Spendelow, M. Chi, Y. Jia, P. Zhang, D. A. Cullen and Z. Xi, *Joule*, 2019, **3**, 124–135.

15 F. Xiao, Q. Wang, G. L. Xu, X. Qin, I. Hwang, C. J. Sun, M. Liu, W. Hua, H. W. Wu, S. Zhu, J. C. Li, J. G. Wang, Y. Zhu, D. Wu, Z. Wei, M. Gu, K. Amine and M. Shao, *Nat. Catal.*, 2022, **5**, 503–512.

16 X. Y. Lang, G. F. Han, B. B. Xiao, L. Gu, Z. Z. Yang, Z. Wen, Y. F. Zhu, M. Zhao, J. C. Li and Q. Jiang, *Adv. Funct. Mater.*, 2015, **25**, 230–237.

17 J. Bai, L. Yang, Z. Jin, J. Ge and W. Xing, *Chinese J. Catal.*, 2022, **43**, 1444–1458.

18 J. Wang, F. Pan, W. Chen, B. Li, D. Yang, P. Ming, X. Wei and C. Zhang, *Electrochem. Energy Rev.*, 2023, **6**, 6.

19 Z. Huang, Y. Wang, J. Xia, S. Hu, N. Chen, T. Ding, C. Zhan, C. W. Pao, Z. Hu and W. H. Huang, *Sci. Adv.*, 2024, **10**, eadq6727.

20 C. L. Yang, L. N. Wang, P. Yin, J. Liu, M. X. Chen, Q. Q. Yan, Z. S. Wang, S. L. Xu, S. Q. Chu, C. Cui, H. Ju, J. Zhu, Y. Lin, J. Shui and H. W. Liang, *Science*, 2021, **374**, 459–464.

21 X. Lu, P. Yang, Y. Wan, H. Zhang, H. Xu, L. Xiao, R. Li, Y. Li, J. Zhang and M. An, *Coord. Chem. Rev.*, 2023, **495**, 215400.

22 H. Huang, K. Shen, F. Chen and Y. Li, *ACS Catal.*, 2020, **10**, 6579–6586.

23 X. Ao, W. Zhang, B. Zhao, Y. Ding, G. Nam, L. Soule, A. Abdelhafiz, C. Wang and M. Liu, *Energy Environ. Sci.*, 2020, **13**, 3032–3040.

24 C. Wan, X. Duan and Y. Huang, *Adv. Energy Mater.*, 2020, **10**, 1903815.

25 W. Xiao, D. Yan, Q. Zhao, D. Bukhvalov and X. Yang, *Appl. Catal., B*, 2024, 123740.

26 Y. Chen, L. Jiao, H. Yan, W. Xu, Y. Wu, L. Zheng, W. Gu and C. Zhu, *Anal. Chem.*, 2021, **93**, 12353–12359.

27 H. Li, G. Wang, F. Zhang, L. Zou, Z. Zou and H. Yang, *J. Phys. Chem. C*, 2020, **124**, 11760–11766.

28 F. Kong, Y. Huang, X. Yu, M. Li, K. Song, Q. Guo, X. Cui and J. Shi, *J. Am. Chem. Soc.*, 2024, **146**, 30078–30090.

29 B. Liu, R. Feng, M. Busch, S. Wang, H. Wu, P. Liu, J. Gu, A. Bahadoran, D. Matsumura and T. Tsuji, *ACS Nano*, 2022, **16**, 14121–14133.

30 B. B. Xu, X. B. Fu, X. M. You, E. Zhao, F. F. Li, Z. Chen, Y. X. Li, X. L. Wang and Y. F. Yao, *ACS Catal.*, 2022, **12**, 6958–6967.

31 J. Gao, X. Zhou, Y. Wang, Y. Chen, Z. Xu, Y. Qiu, Q. Yuan, X. Lin and H. J. Qiu, *Small*, 2022, **18**, 2202071.

32 X. Li, Y. He, S. Cheng, B. Li, Y. Zeng, Z. Xie, Q. Meng, L. Ma, K. Kisslinger and X. Tong, *Adv. Mater.*, 2021, **33**, 2106371.

33 Y. Zeng, J. Liang, C. Li, Z. Qiao, B. Li, S. Hwang, N. N. Kariuki, C. W. Chang, M. Wang and M. Lyons, *J. Am. Chem. Soc.*, 2023, **145**, 17643–17655.

34 F. Zhou, Y. Ruan, M. Zhu, X. Gao, W. Guo, X. Liu, W. Wang, M. Chen, G. Wu and T. Yao, *Small*, 2023, **19**, 2302328.

35 Y. Chen, S. Ji, Y. Wang, J. Dong, W. Chen, Z. Li, R. Shen, L. Zheng, Z. Zhuang and D. Wang, *Angew. Chem., Int. Ed.*, 2017, **56**, 6937–6941.

36 Q. Zhang, T. Shen, M. Song, S. Wang, J. Zhang, X. Huang, S. Lu and D. Wang, *J. Energy Chem.*, 2023, **86**, 158–166.

37 W. J. Zeng, C. Wang, Q. Q. Yan, P. Yin, L. Tong and H. W. Liang, *Nat. Commun.*, 2022, **13**, 7654.

38 J. Li, Z. Xi, Y. T. Pan, J. S. Spendelow, P. N. Duchesne, D. Su, Q. Li, C. Yu, Z. Yin, B. Shen, Y. S. Kim, P. Zhang and S. Sun, *J. Am. Chem. Soc.*, 2018, **140**, 2926–2932.

39 M. Xie, Z. Lyu, R. Chen, M. Shen, Z. Cao and Y. Xia, *J. Am. Chem. Soc.*, 2021, **143**, 8509–8518.

40 C. L. Yang, L. N. Wang, P. Yin, J. Liu, M. X. Chen, Q. Q. Yan, Z. S. Wang, S. L. Xu, S. Q. Chu, C. Cui, H. Ju, J. Zhu, Y. Lin, J. Shui and H. W. Liang, *Science*, 2021, **374**, 459–466.

41 D. S. Choi, A. W. Robertson, J. H. Warner, S. O. Kim and H. Kim, *Adv. Mater.*, 2016, **28**, 7115–7122.

42 C. Yang, Y. Gao, T. Ma, M. Bai, C. He, X. Ren, X. Luo, C. Wu, S. Li and C. Cheng, *Adv. Mater.*, 2023, 2301836.

43 Z. Qiao, C. Wang, C. Li, Y. Zeng, S. Hwang, B. Li, S. Karakalos, J. Park, A. J. Kropf and E. C. Wegener, *Energy Environ. Sci.*, 2021, **14**, 4948–4960.

44 B. Li, L. Wang, H. Liu, J. Chen, J. Xie, Y. Liu and T. C. Lau, *ChemCatChem*, 2023, **15**, e202300023.

45 W. Yang, L. Zou, Q. Huang, Z. Zou, Y. Hu and H. Yang, *J. Electrochem. Soc.*, 2017, **164**, H331–H337.

46 M. R. Subramaniam, R. Shanmugam, S. Sidra, S. Karthikeyan, S. Vijayapradeep, J. Huang, M. Mamlouk, D. H. Kim and J. Y. Dong, *J. Mater. Chem. A*, 2024, **12**, 5967–5979.

47 K. Wan, H. Chen, J. Wang, B. Li, M. Chai, P. Ming and C. Zhang, *J. Catal.*, 2023, **427**, 115124.

48 Y. Wu, P. Ren, R. Li, X. Zheng, C. Bai, Y. Liu, F. Meng, X. Peng, L. Xiao and A. Liu, *J. Power Sources*, 2025, **631**, 236302.

49 S. Zaman, Y. Q. Su, C. L. Dong, R. Qi, L. Huang, Y. Qin, Y. C. Huang, F. M. Li, B. You and W. Guo, *Angew. Chem., Int. Ed.*, 2022, **61**, e202115835.

50 L. Liang, H. Jin, H. Zhou, B. Liu, C. Hu, D. Chen, Z. Wang, Z. Hu, Y. Zhao, H. W. Li, D. He and S. Mu, *Nano Energy*, 2021, **88**, 106221.

51 F. Xiao, Y. Wang, G. L. Xu, F. Yang, S. Zhu, C. J. Sun, Y. Cui, Z. Xu, Q. Zhao and J. Jang, *J. Am. Chem. Soc.*, 2022, **144**, 20372–20384.

52 Y. Han, Y. Xiong, C. Liu, H. Zhang, M. Zhao, W. Chen, W. Chen and W. Huang, *J. Catal.*, 2021, **396**, 351–359.

53 S. Zaman, X. Tian, Y. Q. Su, W. Cai, Y. Yan, R. Qi, A. I. Douka, S. Chen, B. You, H. Liu, S. Ding, X. Guo and B. Y. Xia, *Sci. Bull.*, 2021, **66**, 2207–2216.

54 H. Funke, A. Scheinost and M. Chukalina, *Phys. Rev. B:Condens. Matter Mater. Phys.*, 2005, **71**, 094110.

55 G. Wu, K. L. More, C. M. Johnston and P. Zelenay, *Science*, 2011, **332**, 443–447.

56 M. Wei, L. Huang, L. Li, F. Ai, J. Su and J. Wang, *ACS Catal.*, 2022, **12**, 6478–6485.

57 K. Ehelebe, D. Seeberger, M. T. Paul, S. Thiele, K. J. Mayrhofer and S. Cherevko, *J. Electrochem. Soc.*, 2019, **166**, F1259–F1268.

58 Q. Sun, X. Yue, L. Yu, F. Z. Li, Y. Zheng, M. T. Liu, J. Z. Peng, X. Hu, H. M. Chen and L. Li, *J. Am. Chem. Soc.*, 2024, **146**, 35295–35304.

59 W. Zhou, B. Li, X. Liu, J. Jiang, S. Bo, C. Yang, Q. An, Y. Zhang, M. A. Soldatov and H. Wang, *Nat. Commun.*, 2024, **15**, 6650.

6742 | *Energy Environ. Sci.*, 2025, **18**, 6732–6743

This journal is © The Royal Society of Chemistry 2025

60 W. C. Xu, Z. M. Zhang, C. H. Yang, K. M. Zhao, Y. Wang, N. Tian, Z. Y. Zhou and S. G. Sun, *Electrochem. Commun.*, 2023, **152**, 107516.

61 L. Li, J. Zhu, F. Kong, Y. Wang, C. Kang, M. Xu, C. Du and G. Yin, *Matter*, 2024, **7**, 1517–1532.

62 Y. Zhao, H. C. Chen, X. Ma, J. Li, Q. Yuan, P. Zhang, M. Wang, J. Li, M. Li and S. Wang, *Adv. Mater.*, 2024, **36**, 2308243.

63 Y. H. Wang, J. B. Le, W. Q. Li, J. Wei, P. M. Radjenovic, H. Zhang, X. S. Zhou, J. Cheng, Z. Q. Tian and J. F. Li, *Angew. Chem., Int. Ed.*, 2019, **58**, 16062–16066.

64 J. Behler and M. Parrinello, *Phys. Rev. Lett.*, 2007, **98**, 146401.

65 D. Zhang, H. Bi, F. Z. Dai, W. Jiang, L. Zhang and H. Wang, *arXiv*, 2022, preprint, arXiv:2208.08236, DOI: **10.48550/arXiv.2208.08236**.

66 D. Zhang, X. Liu, X. Zhang, C. Zhang, C. Cai, H. Bi, Y. Du, X. Qin, A. Peng, J. Huang and B. Li, *et al.*, *npj Comput. Mater.*, 2024, **10**, 293.

67 J. K. Nørskov, J. Rossmeisl, A. Logadottir, L. Lindqvist, J. R. Kitchin, T. Bligaard and H. Jonsson, *J. Phys. Chem. B*, 2004, **108**, 17886–17892.

68 J. Chen, Y. Chen, P. Li, Z. Wen and S. Chen, *ACS Catal.*, 2018, **8**, 10590–10598.

69 P. Cai, Y. Li, J. Chen, J. Jia, G. Wang and Z. Wen, *ChemElectroChem*, 2018, **5**, 589–592.

70 Y. Ding, P. Cai and Z. Wen, *Chem. Soc. Rev.*, 2021, **50**, 1495–1511.

71 P. Cai, Y. Li, G. Wang and Z. Wen, *Angew. Chem., Int. Ed.*, 2018, **130**, 3974–3979.

This journal is © The Royal Society of Chemistry 2025

Energy Environ. Sci., 2025, **18**, 6732–6743 | 6743